

**Chiral anomaly and nontrivial Berry phase in the topological nodal-line semimetal SrAs<sub>3</sub>**Linlin An,<sup>1,2</sup> Xiangde Zhu,<sup>1</sup> Wenshuai Gao,<sup>3</sup> Min Wu,<sup>1,2</sup> Wei Ning,<sup>1,\*</sup> and Mingliang Tian<sup>1,3,4,†</sup><sup>1</sup>*Anhui Province Key Laboratory of Condensed Matter Physics at Extreme Conditions, High Magnetic Field Laboratory, Chinese Academy of Sciences, Hefei 230031, Anhui, China*<sup>2</sup>*Department of Physics, University of Science and Technology of China, Hefei 230026, China*<sup>3</sup>*School of Physics and Materials Sciences, Anhui University, Hefei 230601, China*<sup>4</sup>*Collaborative Innovation Center of Advanced Microstructures, Nanjing University, Nanjing 210093, China*

(Received 19 July 2018; published 25 January 2019)

We report the systematic measurement of the magnetoresistance (MR) properties and Hall resistivity of the topological nodal-line semimetal SrAs<sub>3</sub> single crystals. We observed large unsaturated MR accompanied by pronounced Shubnikov-de Hass (SdH) oscillations. Analysis of the SdH oscillations reveals two small frequencies of 1.6 T ( $\alpha$  pocket) and 5.8 T ( $\beta$  pocket). The  $\alpha$  pocket has a nontrivial Berry phase and a small effective mass of  $\sim 0.034m_0$ , while the  $\beta$  pocket has a trivial Berry phase with an effective mass of  $\sim 0.11m_0$ . Hall resistivity measurement reveals the coexistence of a low-concentration hole ( $n_h = 6.45 \times 10^{16} \text{ cm}^{-3}$ ) with high mobility ( $1.68 \times 10^5 \text{ cm}^2 \text{ V}^{-1} \text{ s}^{-1}$ ) and a high-concentration electron ( $n_e = 2.34 \times 10^{17} \text{ cm}^{-3}$ ) with lower mobility ( $9.50 \times 10^3 \text{ cm}^2 \text{ V}^{-1} \text{ s}^{-1}$ ) at 2 K. Furthermore, we observed robust large negative MR in the presence of parallel magnetic and electric fields induced by the chiral magnetic effect.

DOI: [10.1103/PhysRevB.99.045143](https://doi.org/10.1103/PhysRevB.99.045143)**I. INTRODUCTION**

Topological semimetals have attracted considerable interest in the condensed-matter physics research [1–3]. In these materials, the topological semimetallic states are characterized by band touching points or lines between valence and conduction bands in three-dimensional (3D) momentum space. Up to now, several types of topological semimetals have been proposed, including Dirac, Weyl, and nodal-line semimetals [4–9]. In Dirac semimetals, the Dirac points are fourfold degenerate with linear energy dispersion near the points. By breaking either time-reversal or spatial-inversion symmetry, one Dirac point splits into two Weyl points with twofold degeneracy, resulting in transformation of a Dirac semimetal to a Weyl semimetal. By adding parallel electric field and magnetic field between opposite chirality Weyl points, the Weyl fermions pumped from one Weyl point to another of opposite chirality, which leads to chiral anomalies [10,11]. Unlike Dirac and Weyl semimetals with isolated bulk band touching points, topological nodal-line semimetals possess band touching along one-dimensional (1D) loops or lines in 3D momentum space [12–15]. Significant progress has been made in identifying topological semimetals in realistic materials. For example, Dirac semimetals have been proven in Na<sub>3</sub>Bi [16], Cd<sub>3</sub>As<sub>2</sub> [17], etc. The Weyl semimetals have been confirmed in WTe<sub>2</sub> [18], NbP [19], TaAs [20], NbAs [21], and TaP [22], etc., while for nodal-line semimetals, only a few candidates have been identified experimentally, including PtSn<sub>4</sub> [23], PbTaSe<sub>2</sub> [24], and ZrSiX ( $X = \text{S, Se, Te}$ ) [25,26]. Recently, the CaP<sub>3</sub> family of materials, including

CaP<sub>3</sub>, CaAs<sub>3</sub>, SrP<sub>3</sub>, SrAs<sub>3</sub>, and BaAs<sub>3</sub>, was predicted to exist in 3D topological nodal-line semimetal state [27,28]. In these materials, the closed topological nodal line near the Fermi energy is protected by time-reversal symmetry, spatial-inversion symmetry, and mirror symmetry. The nearly flat energy dispersion is an ideal playground for many interaction-induced nontrivial states.

In this work, we report the detailed magnetotransport study of SrAs<sub>3</sub> single crystals. This material was investigated three decades ago and its unusual Hall resistivity and magnetic field-dependent quantum oscillations have been reported [29–31]. However, its topological nature has not been verified yet. In addition, the earlier experimental works only observed one band across the Fermi level [29,30], while the recent theoretical work suggests the existence of at least two bands near the Fermi surface. Here, by the magnetotransport measurements on SrAs<sub>3</sub> single crystals, we observed the large unsaturated magnetoresistance (MR) effect, accompanied by pronounced MR oscillations, i.e., the Shubnikov–de Hass (SdH) effect due to Landau energy splitting. By analyzing the SdH oscillation, we obtained two carriers pockets of Fermi surface that have different effective masses and Berry phase. The Hall resistivity measurement reveals the coexistence of lower concentration hole ( $n_h = 9.63 \times 10^{16} \text{ cm}^{-3}$ ) with high mobility ( $1.68 \times 10^5 \text{ cm}^2 \text{ V}^{-1} \text{ s}^{-1}$ ) and higher-concentration electron ( $n_e = 2.34 \times 10^{17} \text{ cm}^{-3}$ ) with lower mobility ( $\mu_e = 9.35 \times 10^3 \text{ cm}^2 \text{ V}^{-1} \text{ s}^{-1}$ ) at 2 K, indicating that the electron-hole compensation may not be the reason for the large MR in SrAs<sub>3</sub>. Furthermore, we observed robust negative longitudinal magnetoresistance (nLMR) on different samples when the magnetic field is aligned parallel to the applied current (i.e.,  $B \parallel E$ ) in the  $ac$  plane which might be caused by chiral anomaly. Our study provides clear evidence of the existence of Dirac fermions in SrAs<sub>3</sub>.

\*Corresponding author: ningwei@hmf.ac.cn

†Corresponding author: tianml@hmf.ac.cn

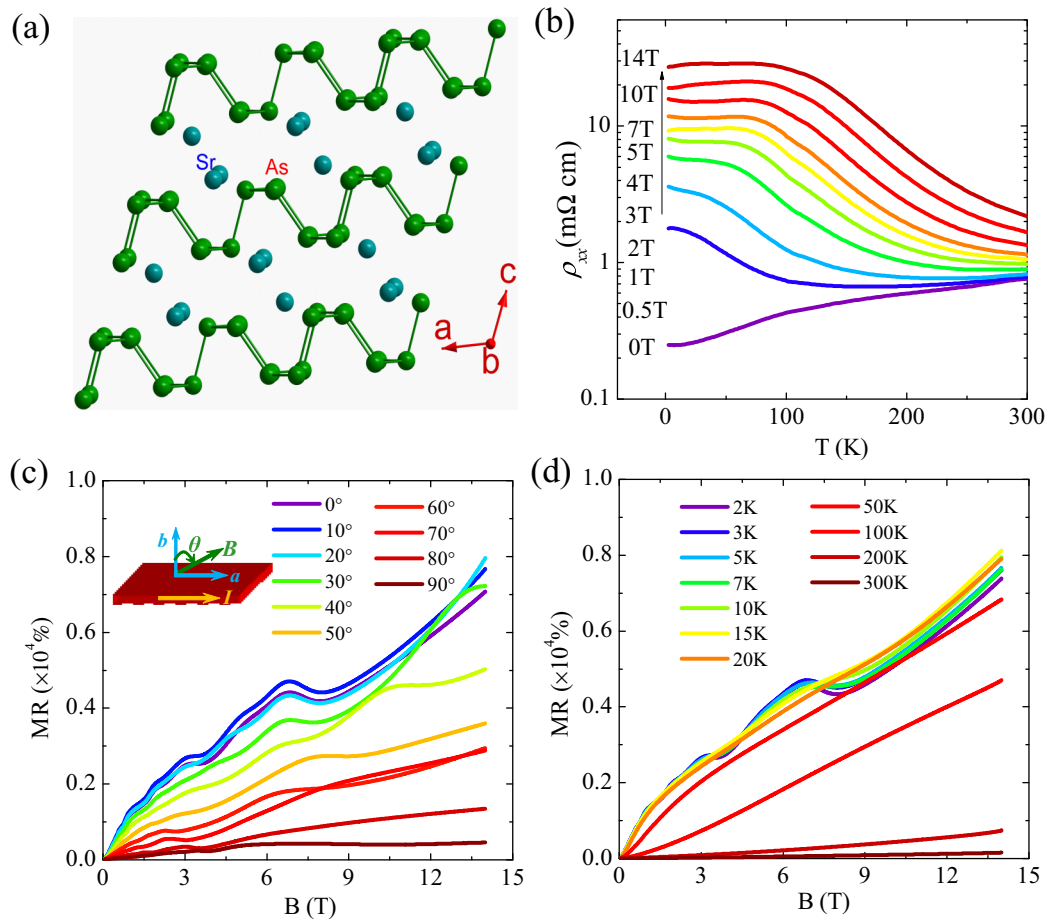


FIG. 1. (a) Crystal structure of  $\text{SrAs}_3$ . (b) Temperature dependence of the resistivity  $\rho_{xx}$  measured under different magnetic fields. (c) Angle dependence of the MR with applied fields rotated from perpendicular ( $\theta = 0^\circ$ ) to parallel ( $\theta = 90^\circ$ ) to the electric current in the ( $a, c$ ) plane. (d) MR measured at different temperatures with fields along the  $b$  axis ( $\theta = 0^\circ$ ).

## II. EXPERIMENTAL METHOD

Single crystals of  $\text{SrAs}_3$  with a metallic luster were grown via the Bi flux method. Raw materials with element Sr, As, and Bi pieces of high purity in mol ratio of 1: 3.1:10 were put in an alumina crucible, and then the crucible was sealed into a quartz tube under vacuum. After slowly heating up to 1123 K and keeping at this temperature for 24 hours, the tube was cooled to 723 K with a rate of 2 K/hour. At this temperature, the tube was taken out of the furnace quickly to separate the crystals from the flux in a centrifuge. The crystal structure of the  $\text{SrAs}_3$  is stacked with 2D puckered polyanionic layers [29]. The  $P$  layers form channels in the  $a$ - $c$  direction and the cations are inserted into the channels, as shown in Fig. 1(a). The space group is  $C2/m$ . The element analysis was performed by using an energy-dispersive x-ray spectroscopy (EDS) in a Helios Nanolab 600i double beam system. The transport properties' measurement was conducted in a physical properties measurement system (PPMS).

## III. RESULTS AND DISCUSSION

Figure 1(b) shows the temperature-dependent resistivity  $\rho_{xx}$  on sample S1 with magnetic field applied perpendicular

to the applied current in the ( $a, c$ ) plane. At zero field,  $\rho_{xx}$  exhibits metallic behavior, which is different from the previous work that the resistivity of the crystals showed a semiconducting-like behavior [29,30,32]. With  $\rho_{xx}(300\text{ K}) = 0.55\text{ m}\Omega\text{ cm}$  and  $\rho_{xx}(2\text{ K}) = 0.14\text{ m}\Omega\text{ cm}$ , the residual resistance ratio (RRR),  $R(300\text{ K})/R(2\text{ K})$  is about 4. When a magnetic field is applied along the  $b$  axis, the temperature-dependent resistivity  $\rho_{xx}$  in the  $ac$  plane increases dramatically, thus resulting in an insulating-like behavior and a plateau in low temperatures when the field is over 0.5 T. Such a magnetic-field-induced metal-insulator-like transition and the resistivity plateau have been observed widely in other topological semimetals [18,19].

Figure 1(c) shows the angle-dependent MR by tilting magnetic fields from the  $b$  axis ( $\theta = 0^\circ$ ) to parallel to the applied current ( $\theta = 90^\circ$ ) in the ( $a, c$ ) plane at 2 K. In order to eliminate the Hall contribution in the data,  $\rho_{xx}(B)$  is symmetrized via  $\rho_{\text{sym}}(H) = [\rho(-H) + \rho(H)]/2$ . For  $B \perp E$  ( $\theta = 0^\circ$ ), the unsaturated MR,  $\text{MR} = [(\rho_{xx}(H) - \rho_{xx}(0))/\rho_{xx}(0)] \times 100\%$ , reaches  $8.1 \times 10^3\%$  at 14 T. As the applied magnetic fields rotate from  $B \perp E$  to  $B \parallel E$  ( $\theta = 90^\circ$ ), the MR dramatically decreases to 470% at 14 T. Figure 1(d) shows the temperature-dependent MR with magnetic field  $B$  fixed along the  $b$  direction ( $\theta = 0^\circ$ ). As temperature increases, the MR ratio reduces

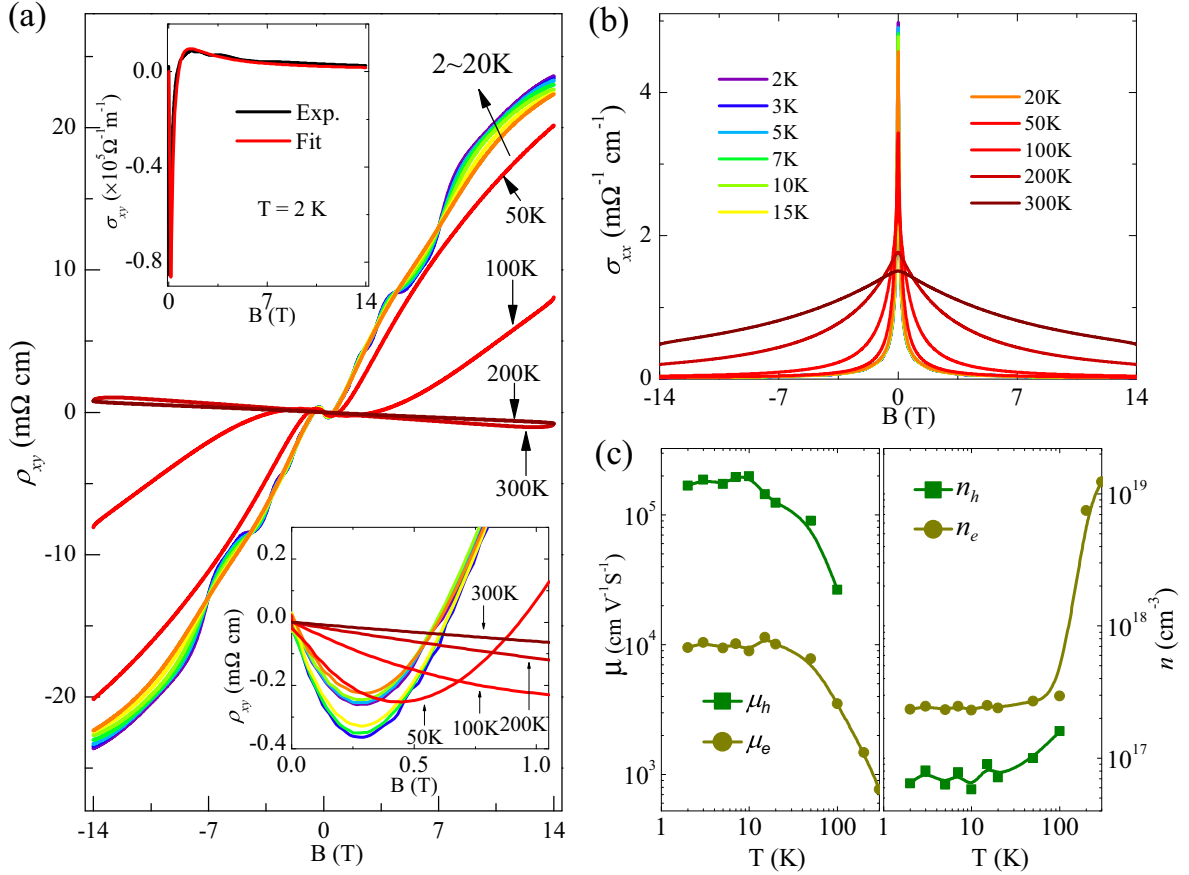


FIG. 2. (a) The Hall resistivity vs magnetic field  $B$  at different temperatures; the blow-up of the plot in low-field range and the Hall conductivity are shown in the insets. (b) The longitudinal conductivity vs magnetic fields at selected temperatures from 2 to 300 K. (c) The concentration and mobility of both carriers are obtained by fitting the Hall conductivity with a two-band model.

gradually and remains 160% at room temperature under 14 T. Beside the large MR, clear MR oscillations can be observed at temperatures less than 20 K.

To obtain the information of the charge carriers of SrAs<sub>3</sub>, we performed detailed Hall resistivity measurement. As shown in Fig. 2(a), above 100 K the Hall resistivity shows a linear behavior with a negative slope, indicating that electron-type carriers dominate the transport. When the temperature is below 100 K,  $\rho_{xy}$  has a negative slope in the low-field range and a positive slope in the higher-field range [as shown in the lower inset of Fig. 2(a)], which implies the coexistence of two types of carriers. We calculated the Hall conductivity [Fig. 2(a)] and longitudinal conductivity [Fig. 2(b)] as  $\sigma_{xy} = \rho_{xy}/(\rho_{xx}^2 + \rho_{xy}^2)$ ,  $\sigma_{xx} = \rho_{xx}/(\rho_{xx}^2 + \rho_{xy}^2)$ , and fit the Hall conductivity with a two-carriers model:

$$\sigma_{xy} = \left[ \frac{n_e \mu_e^2}{1 + (\mu_e B)^2} - \frac{n_h \mu_h^2}{1 + (\mu_h B)^2} \right] eB.$$

Here,  $n_e$  ( $n_h$ ) denotes the carrier concentrations for the electrons (holes), and  $\mu_e$  ( $\mu_h$ ) is the mobility of electrons (holes), respectively. The fitting curves of Hall conductivity at  $T = 2$  K are shown in the insets of Fig. 2(a). The mobility and density of two types of carriers obtained by fitting  $\sigma_{xy}$  are shown

in Fig. 2(c). Both  $\mu_e$  and  $\mu_h$  increase with decreasing temperature and reach  $\mu_h = 1.68 \times 10^5 \text{ cm}^2 \text{ V}^{-1} \text{ s}^{-1}$  and  $\mu_e = 9.5 \times 10^3 \text{ cm}^2 \text{ V}^{-1} \text{ s}^{-1}$  at  $T = 2$  K. As temperature decreases, the density of the two types of carriers reduces gradually and reaches  $n_h = 9.63 \times 10^{16} \text{ cm}^{-3}$  and  $n_e = 2.34 \times 10^{17} \text{ cm}^{-3}$  at 2 K.

In order to obtain more information on the electronic structure of the SrAs<sub>3</sub>, we now turn to the detailed investigation of the quantum oscillations. Figure 3(a) shows the longitudinal conductivity versus magnetic fields at selected temperatures from 2 to 10 K. In Fig. 3(b), we present the oscillatory component of the longitudinal conductivity,  $\Delta\sigma_{xx}$ , versus  $1/B$  after subtracting a smoothing background. The quantum oscillations can be traced from a magnetic field as low as 0.3 T. The fast Fourier transform (FFT) spectra of the oscillations are shown in Fig. 3(c). The spectra reveal two principal frequencies,  $F_\alpha = 1.6$  T and  $F_\beta = 5.8$  T, with a harmonic frequency  $F_{2\alpha} = 3.2$  T, indicating at least two pockets across the Fermi surface. According to the Onsager relation  $F = (\hbar/2\pi e)S_F$ , where  $F$  is the frequency of oscillations, the cross section of the Fermi surface,  $S_F$ , is determined to be  $\sim 1.52 \times 10^{-4}$  and  $\sim 5.52 \times 10^{-4} \text{ \AA}^{-2}$  for the  $\alpha$  and  $\beta$  bands, respectively. The corresponding Fermi wave vectors  $k_F$  are  $\sim 0.00696$  and  $\sim 0.0133 \text{ \AA}^{-1}$ , respectively.

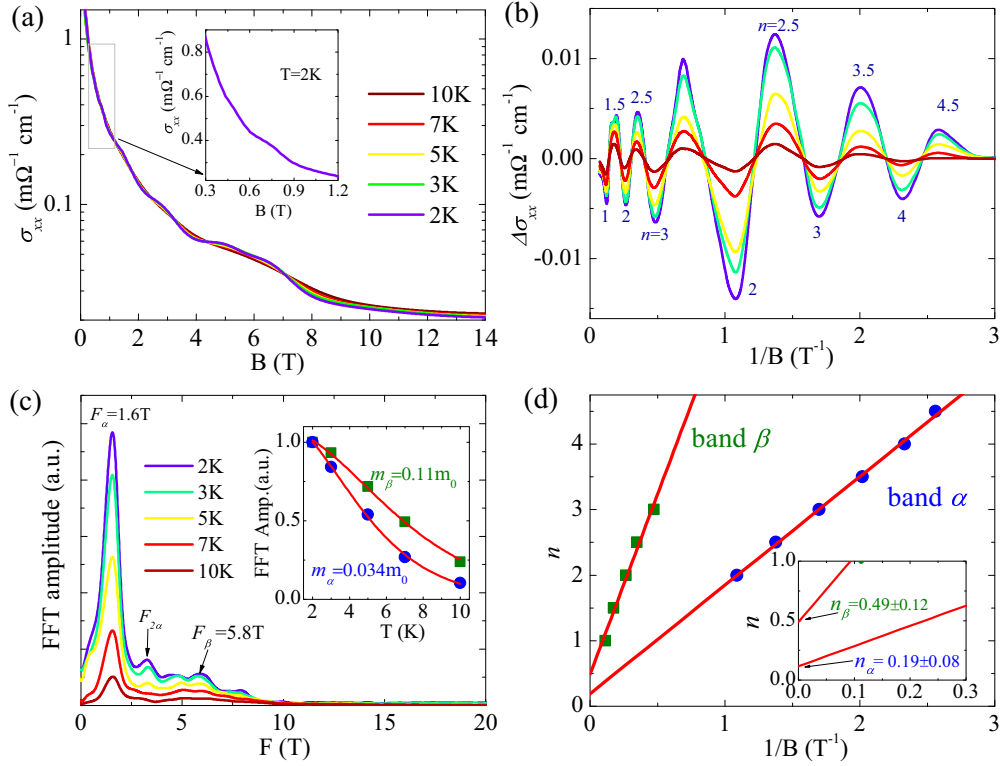


FIG. 3. (a) The longitudinal conductivity  $\sigma_{xx}$  vs magnetic fields at selected temperatures from 2 to 10 K. The inset shows the enlargement of the  $\sigma_{xx}$  at 2 K below 1.2 T. (b) The SdH oscillatory component  $\Delta\sigma_{xx}$  as a function of  $1/B$  obtained after subtracting a smoothing background; (c) corresponding FFT spectra of the oscillations. Two fundamental frequencies of 1.6 and 5.8 T can be identified. The inset shows the temperature dependence of the relative amplitudes of the SdH oscillation. The solid lines are the results of the LK formula fitting. (d) Landau-level (LL) indices extracted from the SdH oscillation plotted as a function of  $1/B$ .

The SdH oscillations can be described by the Lifshitz-Kosevich (LK) formula [33],

$$\frac{\Delta\rho(T, B)}{\rho(B=0)} \propto \frac{2\pi^2 k_B T / \hbar\omega_c}{\sinh[2\pi^2 k_B T / \hbar\omega_c]} \exp(-2\pi^2 k_B T_D / \hbar\omega_c) \times \cos\left[2\pi\left(\frac{F}{B} + \gamma - \delta\right)\right], \quad (1)$$

where  $k_B$  is the Boltzmann constant,  $\hbar$  is the Planck's constant and  $\omega_c = eB/m^*$  is the cyclotron frequency, with  $m^*$  the effective cyclotron mass at the Fermi energy,  $T_D$  is the Dingle temperature, and the effective mass can be obtained from the fitting of the temperature dependence of FFT amplitudes to the thermal damping term of the LK formula,  $\frac{2\pi^2 k_B T / \hbar\omega_c}{\sinh[2\pi^2 k_B T / \hbar\omega_c]}$ . As shown in the inset of Fig. 3(c), the fitting yields effective masses of  $m_\alpha^* = 0.034m_0$  and  $m_\beta^* = 0.11m_0$  ( $m_0$  is the free electron mass) for the  $\alpha$  and  $\beta$  bands, respectively. From the cyclotron effective mass,  $v_F = \hbar k_F / m^*$ , the obtained Fermi velocity is  $v_\alpha = 2.37 \times \frac{10^5 \text{ m}}{\text{s}}$ , and  $v_\beta = 1.29 \times 10^5 \text{ m/s}$  for two bands. Thus, the estimated Fermi energy  $E_F = \hbar^2 k_F^2 / m^*$  is  $E_F^\alpha = 10.88 \text{ meV}$  and  $E_F^\beta = 11.21 \text{ meV}$ , respectively.

To gain deeper insight into the topological nature of the bands, the Landau level (LL) index fan diagram is usually used to extract the Berry phase for topological materials. Under perpendicular magnetic fields, the SdH quantum oscillation due to the quantized closed orbits follows the Lifshitz-Onsager quantization rule [34], i.e.,  $\cos[2\pi(\frac{F}{B} + \gamma - \delta)]$ ,

where  $\gamma$  is the Onsager phase factor that is related to Berry phase through  $\gamma = 1/2 - \phi_B/2\pi$ . In a conventional electron system, the Berry phase  $\phi_B = 0$ , hence  $\gamma = 1/2$ , while for massless Dirac materials with linear band dispersion, the  $k$ -space cyclotron orbits enclose a Dirac point so that there exists a “zero mode” that does not shift with  $B$ , resulting in a nontrivial Berry phase:  $\phi = \pi$ , which makes  $\gamma = 0$ .  $\delta$  is the phase shift determined by the dimension of the Fermi surface; it is 0 for 2D and  $\pm 1/8$  for 3D cases (the sign “ $\pm$ ” closely depends on the extreme cross-section area of the Fermi surface maximal or minimal, respectively). Here the valley of the oscillations was defined as integer indices  $n$ , while the peaks were defined as half indices  $n + 1/2$  [35]. Figure 3(d) shows the  $n$  versus  $1/B$  curves, and the linear fittings give the intercepts of  $\gamma_\alpha = 0.19 \pm 0.08$  and  $\gamma_\beta = 0.49 \pm 0.12$  for the  $\alpha$  and  $\beta$  bands. Since  $\gamma_\alpha = 0.19 \pm 0.08$  is close to  $1/8$  within experimental error, indicating the nontrivial Berry phase of the electronic state, while  $\gamma_\beta$  is close to  $-1/2$  suggests the trivial electronic state of this band. We note that due to the limit of subtracting of the background or the interference of multiple bands on the quantum oscillations, the nontrivial Berry phase obtained from the LL index fan diagram might not be very accurate. Further angle-resolved photoemission spectroscopy (ARPES) measurements might be very helpful for verification of the topological nature of SrAs<sub>3</sub>.

Figure 4(a) shows the angle-dependent longitudinal MR of another sample S2 at 2 K with the magnetic field oriented from perpendicular to parallel to the current direction along the  $a$

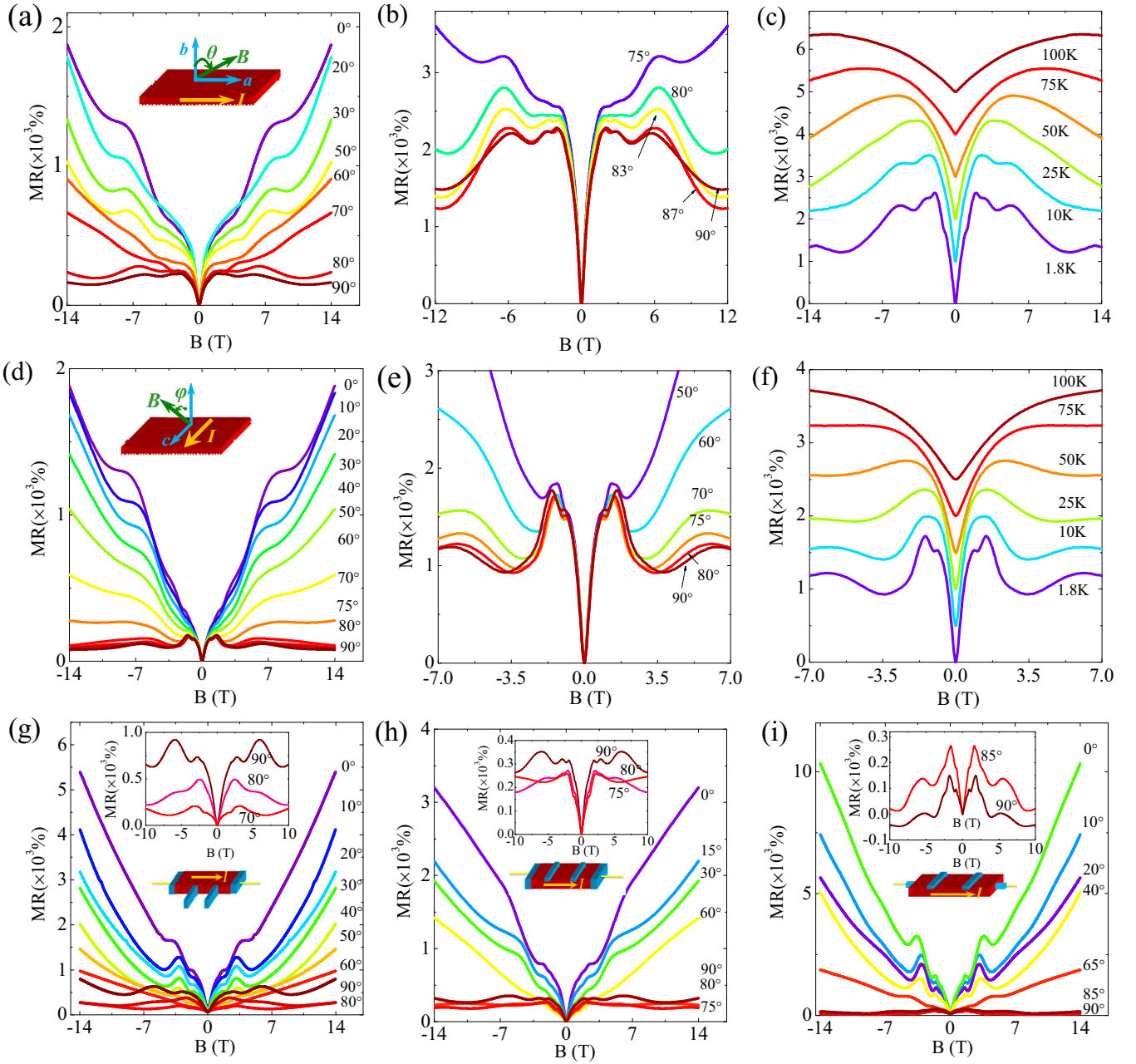


FIG. 4. (a),(d) Longitudinal MR of sample S2 measured at 2 K while tilting the magnetic field from  $B \perp E$  ( $\theta = 0^\circ$ ) to  $B \parallel E$  ( $\theta = 90^\circ$ ). (b),(e) The MR measured in high angles at 2 K. (c),(f) The MR measured at  $B \parallel E$  at different temperatures. (g) The longitudinal MR of sample S3 measured at 2 K with current applied along the  $c$  axis. The current contacts fully covered the sample ends and the voltage contacts were placed at the sample side. (h) The current contacts fully covered the sample ends and the voltage contacts crosses the width of the sample. (i) The voltage contacts cross the width of the sample while the current point contacts with the sample ends.

axis. To eliminate the possible influence of the Hall signal, the  $R_{xx}$  data were averaged by measuring the resistance over positive and negative field directions. With increasing  $\theta$ , the MR decreases dramatically. When the field is parallel to the current ( $\theta = 90^\circ$ ), a clear negative longitudinal MR is observed, as shown in Fig. 4(b). At low-field range ( $B < 1$  T), the MR shows a sharp dip with positive slope which may be ascribed to a weak antilocalization (WAL) effect as a result of strong spin-orbit coupling in  $\text{SrAs}_3$ . Such WAL behavior has been observed in topological insulators [36] and graphene [37], in which the magnetotransport is dominated by Dirac fermions.

When the field increases, the MR becomes negative and then positive in the high-field range. The negative MR behavior can be observed with  $\theta > 80^\circ$ . Meanwhile, the negative LMR is suppressed by increasing temperature and disappears above 75 K, as shown in Fig. 4(c). We have repeated the measurement with current applied along the  $c$  axis on the same sample, as shown in Figs. 4(d)–4(f). A similar WAL effect at the low-field range and nLMR with  $\varphi > 60^\circ$  were seen. The nLMR is also suppressed by increasing temperature above 75 K.

Physically, the nLMR in topological metals can actually be induced by the axial anomaly due to inhomogeneous

current distribution (i.e., the “current jetting” effect) when the sizes of the current contacts are much smaller than the front and end of the materials. In order to exclude the possible influence of the current jetting effect on the nLMR in SrAs<sub>3</sub>, we have measured the MR on another sample S3 with different voltage and current setup process, as shown in Figs. 4(g)–4(i). Figure 4(g) and 4(h) show the results in which the current contacts covered the samples end, while the voltage contacts were placed at the sample side and crossed the width of the sample, respectively. Figure 4(i) shows the voltage contacts cross the width of the sample while the current point contacts with the sample ends. In all three measurement setup processes, the nLMR can be observed clearly when the magnetic field is parallel to the current ( $\theta = 90^\circ$ ), indicating that the nLMR is not caused by the magnetic-field-induced current jetting effect. Such an angle-sensitive nLMR behavior has been observed in other Dirac/Weyl semimetals [38–40], and it was regarded as one of the most prominent signatures for the chiral anomaly. The observed robust negative MR in SrAs<sub>3</sub> provides a clear evidence of the topological nature of SrAs<sub>3</sub>.

#### IV. CONCLUSIONS

In conclusion, detailed magnetotransport measurements were performed on SrAs<sub>3</sub> single crystals. The crystals ex-

hibit very large MR without saturation. Analysis of SdH oscillations reveals the existence of two Fermi pockets with extremely small extremal area. One pocket has a nontrivial Berry phase and a small effective mass of  $\sim 0.034m_0$ , while another pocket has a trivial Berry phase with an effective mass of  $\sim 0.11m_0$ . Hall resistivity measurement suggests that both electron and hole carriers contribute to the MR, but the carrier concentration for electrons is much higher than that for holes, indicating that this is an uncompensated system. Additionally, very robust negative MR behavior was observed with current applied along different axes. Our research proves clear evidence of the existence of Dirac fermions in SrAs<sub>3</sub>.

#### ACKNOWLEDGMENTS

This work was supported by the National Key Research and Development Program of China, Grant No. 2016YFA0401003, the Natural Science Foundation of China (Grants No. 11774353, No. 11574320, No. 11374302, No. U1432251, and No. U1732274), the International Users of Hefei Science Center of CAS (Grant No. 2016HSC-IU009), the Innovative Program of Development Foundation of Hefei Center for Physical Science and Technology (Grant No. 2018CXFX002), and the CAS/SAFEA international partnership program for creative research teams of China.

- 
- [1] C.-K. Chiu, J. C. Teo, A. P. Schnyder, and S. Ryu, Classification of topological quantum matter with symmetries, *Rev. Mod. Phys.* **88**, 035005 (2016).
- [2] A. Bansil, H. Lin, and T. Das, Colloquium: Topological band theory, *Rev. Mod. Phys.* **88**, 021004 (2016).
- [3] X. Dai, Quantum Materials: Weyl fermions go into orbit, *Nat. Phys.* **12**, 727 (2016).
- [4] X. G. Wan, A. M. Turner, A. Vishwanath, and S. Y. Savrasov, Topological semimetal and Fermi-arc surface states in the electronic structure of pyrochlore iridates, *Phys. Rev. B* **83**, 205101 (2011).
- [5] M. Orlita, D. M. Basko, M. S. Zholudev, F. Teppe, W. Knap, V. I. Gavrilenko, N. N. Mikhailov, S. A. Dvoretiskii, P. Neugebauer, C. Faugeras, C. Faugeras, A.-L. Barra, G. Martinez, and M. Potemski, Observation of three-dimensional massless Kane fermions in a zinc-blende crystal, *Nat. Phys.* **10**, 233 (2014).
- [6] S. M. Young, S. Zaheer, J. C. Y. Teo, C. L. Kane, E. J. Mele, and A. M. Rappe, Dirac semimetal in three dimensions, *Phys. Rev. Lett.* **108**, 140405 (2012).
- [7] Z. J. Wang, Y. Sun, X. Q. Chen, C. Franchini, G. Xu, H. M. Weng, X. Dai, and Z. Fang, Dirac semimetal and topological phase transitions in A<sub>3</sub>Bi (A = Na, K, Rb), *Phys. Rev. B* **85**, 195320 (2012).
- [8] Z. J. Wang, H. M. Weng, Q. S. Wu, X. Dai, and Z. Fang, Three-dimensional Dirac semimetal and quantum transport in Cd<sub>3</sub>As<sub>2</sub>, *Phys. Rev. B* **88**, 125427 (2013).
- [9] H. Weng, Y. Liang, Q. Xu, R. Yu, Z. Fang, X. Dai, and Y. Kawazoe, Topological Node-line semimetal in three dimensional graphene networks, *Phys. Rev. B* **92**, 045108 (2015).
- [10] H. B. Nielsen and M. Ninomiya, The Adler-Bell-Jackiw anomaly and Weyl fermions in a crystal, *Phys. Lett. B* **130**, 389 (1983).
- [11] D. T. Son and B. Z. Spivak, Chiral anomaly and classical negative magnetoresistance of Weyl metals, *Phys. Rev. B* **88**, 104412 (2013).
- [12] R. Yu, H. Weng, Z. Fang, X. Dai, and X. Hu, Topological Node-Line Semimetal and Dirac Semimetal State in Antiperovskite Cu<sub>3</sub>PdN, *Phys. Rev. Lett.* **115**, 036807 (2015).
- [13] Q.-F. Liang, J. Zhou, R. Yu, Z. Wang, and H. Weng, Node-surface and node-line fermions from nonsymmorphic lattice symmetries, *Phys. Rev. B* **93**, 085427 (2016).
- [14] H. Huang, J. Liu, D. Vanderbilt, and W. Duan, Topological nodal-line semimetals in alkaline-earth stannides, germanides, and silicides, *Phys. Rev. B* **93**, 201114 (2016).
- [15] X. B. Wang, X. M. Ma, E. Emmanouilidou, B. Shen, C. H. Hsu, C. S. Zhou, Y. Zuo, R. R. Song, S. Y. Xu, G. Wang, L. Huang, N. Ni, and C. Liu, Topological surface electronic states in candidate nodal-line semimetal CaAgAs, *Phys. Rev. B* **96**, 161112(R) (2017).
- [16] Z. K. Liu, B. Zhou, Y. Zhang, Z. J. Wang, H. M. Weng, D. Prabhakaran, S.-K. Mo, Z. X. Shen, Z. Fang, X. Dai, Z. Hussain, and Y. L. Chen, Discovery of a three-dimensional topological Dirac semimetal, Na<sub>3</sub>Bi, *Science* **343**, 864 (2014).
- [17] Z. K. Liu, J. Jiang, B. Zhou, Z. J. Wang, Y. Zhang, H. M. Weng, D. Prabhakaran, S.-K. Mo, H. Peng, P. Dudin, T. Kim, M. Hoesch, Z. Fang, X. Dai, Z. X. Shen, D. L. Feng, Z. Hussain, and Y. L. Chen, A stable three-dimensional topological Dirac semimetal Cd<sub>3</sub>As<sub>2</sub>, *Nat. Mater.* **13**, 677 (2014).
- [18] M. N. Ali, J. Xiong, S. Flynn, J. Tao, Q. D. Gibson, L. M. Schoop, T. Liang, N. Haldolaarachchige, M. Hirschberger, N. P. Ong, and R. J. Cava, Large, non-saturating magnetoresistance in WTe<sub>2</sub>, *Nature (London)* **514**, 205 (2014).

- [19] C. Shekhar, A. K. Nayak, Y. Sun, M. Schmidt, M. Nicklas, I. Leermakers, U. Zeitler, Y. Skourski, J. Wosnitza, Z. K. Liu, Y. L. Chen, W. Schnelle, H. Borrmann, Y. Grin, C. Felser, and B. H. Yan, Extremely large magnetoresistance and ultrahigh mobility in the topological Weyl semimetal candidate NbP, *Nat. Phys.* **11**, 645 (2015).
- [20] S. Y. Xu, I. Belopolski, N. Alidoust, M. Neupane, G. Bian, C. L. Zhang, R. Sankar, G. Q. Chang, Z. J. Yuan, C. C. Lee, S. M. Huang, H. Zheng, J. Ma, D. S. Sanchez, B. K. Wang, A. Bansil, F. C. Chou, P. P. Shibayev, H. Lin, S. Jia, and M. Z. Hasan, Discovery of a Weyl fermion semimetal and topological Fermi arcs, *Science* **349**, 613 (2015).
- [21] S. Y. Xu, N. Alidoust, I. Belopolski, Z. J. Yuan, G. Bian, T.-R. Chang, H. Zheng, V. N. Strocov, D. S. Sanchez, G. Q. Chang *et al.*, Discovery of a Weyl fermion state with Fermi arcs in niobium arsenide, *Nat. Phys.* **11**, 748 (2015).
- [22] S. Y. Xu, I. Belopolski, D. S. Sanchez, C. Zhang, G. Chang, C. Guo, G. Bian, Z. Yuan, H. Lu, T.-R. Chang, P. P. Shibayev, M. L. Prokopovych, N. Alidoust, H. Zheng, C.-C. Lee, S.-M. Huang, R. Sankar, F. C. Chou, C.-H. Hsu, H.-T. Jeng *et al.*, Experimental discovery of a topological Weyl semimetal state in TaP, *Sci. Adv.* **1**, e1501092 (2015).
- [23] Y. Wu, L. L. Wang, E. Mun, D. D. Johnson, D. X. Mou, L. N. Huang, Y. B. Lee, S. L. Bud'ko, P. C. Canfield, and A. Kaminski, Dirac node arcs in PtSn<sub>4</sub>, *Nat. Phys.* **12**, 667 (2016).
- [24] G. Bian, T.-R. Chang, R. Sankar, S.-Y. Xu, H. Zheng, T. Neupert, C.-K. Chiu, S.-M. Huang, G. Chang, I. Belopolski *et al.*, Topological nodal-line fermions in spin-orbit metal PbTaSe<sub>2</sub>, *Nat. Commun.* **7**, 10556 (2016).
- [25] L. M. Schoop, M. N. Ali, C. Straßer, A. Topp, A. Varykhalov, D. Marchenko, V. Duppel, S. S. P. Parkin, B. V. Lotsch, and C. R. Ast, Dirac cone protected by non-symmorphic symmetry and three-dimensional Dirac line node in ZrSiS, *Nat. Commun.* **7**, 11696 (2016).
- [26] J. Hu, Z. J. Tang, J. Y. Liu, X. Liu, Y. L. Zhu, D. Graf, K. Myhro, S. Tran, C. N. Lau, J. Wei, and Z. Q. Mao, Evidence of Topological Nodal-Line Fermions in ZrSiSe and ZrSiTe, *Phys. Rev. Lett.* **117**, 016602 (2016).
- [27] Q. Xu, R. Yu, Z. Fang, X. Dai, and H. M. Weng, Topological Nodal Line Semimetals in CaP<sub>3</sub> family of materials, *Phys. Rev. B* **95**, 045136 (2017).
- [28] Y. Quan, Z. P. Yin, and W. E. Pickett, Single Nodal Loop of Accidental Degeneracies in Minimal Symmetry: Triclinic CaAs<sub>3</sub>, *Phys. Rev. Lett.* **118**, 176402 (2017).
- [29] W. Bauhofer, M. Wittmann, and H. Schnering, Structure, electrical and magnetic properties of CaAs<sub>3</sub>, SrAs<sub>3</sub>, BaAs<sub>3</sub> and EuAs<sub>3</sub>, *J. Phys. Chem. Solids* **42**, 687 (1981).
- [30] M. Möllendorf and W. Bauhofer, First-order longitudinal Hall effect, *Phys. Rev. B* **30**, 1099 (1984).
- [31] P. J. Klar and W. Bauhofer, Galvanomagnetic properties and band structure of monoclinic SrAs<sub>3</sub>, *Phys. Rev. B* **50**, 5180 (1994).
- [32] S. C. Li, Z. P. Guo, D. Z. Fu, X. C. Pan, J. H. Wang, K. J. Ran, S. Bao, Z. Ma, Z. W. Cai, R. Wang, R. Yu, J. Sun, F. Q. Song, and J. S. Wen, Evidence for a Dirac nodal-line semimetal in SrAs<sub>3</sub>, *Sci. Bull.* **63**, 535 (2018).
- [33] I. M. Lifshits and A. M. Kosevich, On the theory of magnetic susceptibility in metals at low temperatures, *Sov. Phys. JETP* **2**, 636 (1956).
- [34] D. Shoenberg, *Magnetic Oscillations in Metals* (Cambridge University Press, Cambridge, 1984).
- [35] Y. Ando, Topological insulator materials, *J. Phys. Soc. Jpn.* **82**, 102001 (2013).
- [36] H. T. He, G. Wang, T. Zhang, I. K. Sou, G. K. L. Wong, J. N. Wang, H. Z. Lu, S. Q. Shen, and F. C. Zhang, Impurity Effect on Weak Antilocalization in the Topological Insulator, *Phys. Rev. Lett.* **106**, 166805 (2012).
- [37] X. S. Wu, X. B. Li, Z. M. Song, C. Berger, and W. A. de Heer, Weak Antilocalization in Epitaxial Graphene: Evidence for Chiral Electrons, *Phys. Rev. Lett.* **98**, 136801 (2007).
- [38] J. Xiong, S. K. Kushwaha, T. Liang, J. W. Krizan, M. Hirschberger, W. Wang, R. J. Cava, and N. P. Ong, Evidence for the chiral anomaly in the Dirac semimetal Na<sub>3</sub>Bi, *Science* **350**, 413 (2015).
- [39] C.-Z. Li, L.-X. Wang, H. W. Liu, J. Wang, Z.-M. Liao, and D.-P. Yu, Giant negative magnetoresistance induced by the chiral anomaly in individual Cd<sub>3</sub>As<sub>2</sub> nanowires, *Nat. Commun.* **6**, 10137 (2015).
- [40] G. L. Zheng, J. Lu, X. D. Zhu, W. Ning, Y. Y. Han, H. W. Zhang, J. L. Zhang, C. Y. Xi, J. J. Yang, H. F. Du, K. Yang, Y. H. Zhang, and M. L. Tian, Transport evidence for the three-dimensional Dirac semimetal phase in ZrTe<sub>5</sub>, *Phys. Rev. B* **93**, 115414 (2016).